remote sensing

MDPI

Article

Assessing Single-Polarization and Dual-Polarization TerraSAR-X Data for Surface Water Monitoring

Katherine Irwin [1], Alexander Braun [1,*], Georgia Fotopoulos [1], Achim Roth [2] and Birgit Wessel [2]

[1] Department of Geological Sciences and Geological Engineering, Queen's University, Kingston, ON K7L 3N6, Canada; 0kei@queensu.ca (K.I.); gf26@queensu.ca (G.F.)

[2] German Aerospace Center (DLR), D-82234 Wessling, Germany; Achim.Roth@dlr.de (A.R.); Birgit.Wessel@dlr.de (B.W.)

* Correspondence: braun@queensu.ca; Tel.: +1-613-533-6621

Received: 5 May 2018; Accepted: 13 June 2018; Published: 14 June 2018

Abstract: Three synthetic aperture radar (SAR) data classification methodologies were used to assess the ability of single-polarization and dual-polarization TerraSAR-X (TSX) data to classify surface water, including open water, ice, and flooded vegetation. Multi-polarization SAR observations contain more information than single-polarization SAR, but the availability of multi-polarization data is much lower, which limits the temporal monitoring capabilities. The study area is a principally natural landscape centered on a seasonally flooding river, in which four TSX dual-co-polarized images were acquired between the months of April and June 2016. Previous studies have shown that single-polarization SAR is useful for analyzing surface water extent and change using grey-level thresholding. The H-Alpha–Wishart decomposition, adapted to dual-polarization data, and the Kennaugh Element Framework were used to classify areas of water and flooded vegetation. Although grey-level thresholding was able to identify areas of water and non-water, the percentage of seasonal change was limited, indicating an increase in water area from 8% to 10%, which is in disagreement with seasonal trends. The dual-polarization methods show a decrease in water over the season and indicate a decrease in flooded vegetation, which agrees with expected seasonal variations. When comparing the two dual-polarization methods, a clear benefit of the Kennaugh Elements Framework is the ability to classify change in the transition zones of ice to open water, open water to marsh, and flooded vegetation to land, using the differential Kennaugh technique. The H-Alpha–Wishart classifier was not able to classify ice, and misclassified fields and ice as water. Although single-polarization SAR was effective in classifying open water, the findings of this study confirm the advantages of dual-polarization observations, with the Kennaugh Element Framework being the best performing classification framework.

Keywords: synthetic aperture radar; PolSAR; TerraSAR-X; surface water monitoring; flooded vegetation; classification; segmentation

1. Introduction

Synthetic aperture radar (SAR) is an active remote sensing technique and can penetrate cloud cover and operate during the day or night. Often, flood events occur during unfavourable weather conditions when optical visibility is low, which allows SAR to be a useful sensor for surface water classification [1]. SAR missions and products vary in polarization, incidence angle, frequency, and resolution, which allows the user to select the most suitable SAR observations to the application at hand, which in this case is the classification of surface water and its varying states. Currently, there exists a trade-off between spatio-temporal coverage and information content with respect to single-polarization and multi-polarization SAR data. While multi-polarization contains more

information about the scattering mechanism of the target, the temporal coverage over a single target is limited and prohibits monitoring over regional scales. Many studies addressed the use of single- or multi-polarization SAR individually using diverse classification algorithms, but few addressed the comparison of single- and multi-polarization SAR data for surface water monitoring [1–4]. These comparative studies mainly address single-polarization and quad-polarization processing methods, or address which dual-polarization channels are most effective for surface water monitoring, but lack discussion of the dual-polarization processing methods. In this study, there are three main objectives. The first is to create classified models of surface water using both single- and dual-polarization TerraSAR-X (TSX) data. The second is to compare these models to better understand the extent of the limitations of single-polarization data and to what extent they are aided by dual-polarization data. The third objective is to create a surface water extent time series from the initial snow melt period into spring, to demonstrate the feasibility of near-continuous surface water monitoring from space. The current fleet of ~10 civil SAR missions in orbit and the planned missions up to 2020 provide and will continue to provide an unprecedented amount of observations in the X-, C-, and L-band, mostly in single-polarization mode, which will lead to near-continuous monitoring capabilities. Different radar frequencies (X-, C-, and L-band) interact differently with vegetation, and thus wetlands. The shorter the wavelength (X-band) of the radar, the less penetration into the canopy, while L-band radar penetrates through the canopy to the ground. However, X-band SAR is the preferred sensor for open water mapping as the shorter wavelength leads to increased diffuse scattering when compared with the C-band and L-band radar, which suffer from specular reflections leading to low energy return.

Previous studies have shown that single-polarization SAR data are a viable technology for analyzing surface water extent and spatio-temporal change [4–16]. Single-polarization SAR provides one channel of intensity data in either HH (horizontal linear transmission and horizontal linear reception), HV (horizontal linear transmission and vertical linear reception), VH (vertical linear transmission and horizontal linear reception), or VV (vertical linear transmission and vertical linear reception). One of the most common and effective classification techniques is grey-level thresholding, which can be applied to differentiate areas of water and non-water [4,17]. This has proved successful to delineate open water bodies, but limitations arise with more heterogeneous targets, such as ice covered water bodies and surface water beneath vegetation—which are abundant in Canada, with approximately 14% of the Canadian landscape being covered in wetlands [4]. Vegetation cover leads to misclassification due to shadow and layover effects, and ice can often be misclassified because of the similar backscatter response to rough surface water [4,9]. Wind effects can also lead to misclassification causing water to be mistaken as land, rough vegetation, or ice [4]. Multi-temporal SAR acquisitions often occur during ice-off conditions to avoid misclassification. However, it is important to document the initial stages of snowmelt and spring flooding, because the subsequent hydrological conditions rely on this initial process [4]. The limitations of single-polarization SAR could be aided by the use of dual-polarization SAR, which provides two channels of intensity and phase information (HH/HV, VV/VH, or HH/VV). Having two channels of intensity and phase information allows for discerning among scattering mechanisms, such as surface scattering, double bounce, and volume scattering. Dual-polarization SAR data can be used to distinguish ice and vegetated areas from open water, while those land cover types often lead to misclassification in single-polarization data [4,18,19]. Several studies have identified the significant double-bounce component originating from flooded vegetation and hence, quad-polarization SAR must often be used for classification [20–22]. Quad-polarization data are often not available, while dual-polarization have been demonstrated to be sufficient [18,23–26].

2. Data Description and Methodology

2.1. Study Area and Data Description

The ~6 km × 12 km study area is located south of Lac-Simon in Quebec, Canada (Figure 1). This area was chosen because it is a principally natural landscape with open bodies of water, marshland, and forested areas. Most importantly, it includes the Ruisseau Schryer, which flows from A (Lac-Schryer) to B (Baie-de-l'Ours in Lac-Simon) in Figure 1, and is flooded during the snowmelt each year. This could affect the urban areas located near the river, including the town of Montpellier located on the north side of the stream. Montpellier experienced flooding due to seasonally high water levels and overflowing rivers in April of 2017. These events threatened and damaged multiple homes and a state of emergency was declared in towns near to Montpellier. The orange box in Figure 1 zooms in on the river entering Baie-de-l'Ours, showing a distinct flood plain surrounding both sides of the meandering river.

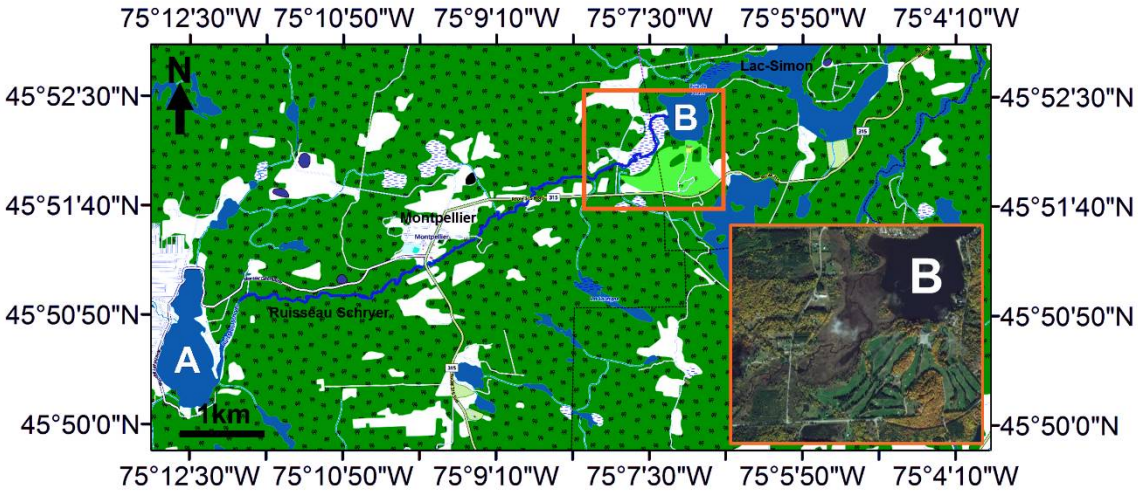

Figure 1. Map of study area showing the town of Montpellier, southern extent of Lac-Simon, and stream (Ruisseau Schryer) flowing from A (Lac-Schryer) to B (Baie-de-l'Ours). Base map is provided by the Quebec Ministry of Energy and Natural Resources (MERN) showing urban areas (white), water (blue), forest (dotted green), low vegetation (tan), golf course (light green), and marshlands (dashed areas). Zoomed in orange box of Google Earth imagery from July 2017 shows a flood plain surrounding the stream entering Lac-Simon at B.

Four TSX dual-co-polarization (HH/VV) strip-map mode scenes were acquired through the spring and summer of 2016. Each scene has an areal extent of 15 km by 50 km and a slant range and azimuth resolution of 1.2 m and 6.6 m, respectively. The incidence angle was chosen to be low enough to be able to penetrate the vegetation types on site and cover the target area. Details of each product are provided in Table 1.

Table 1. Specifications of the four dual-polarization TerraSAR-X strip-map beam mode scenes used herein. VV—vertical linear transmission and vertical linear reception; HH—horizontal linear transmission and horizontal linear reception.

ID	Date (2016)	Mode	Polarization	Product	Look Direction	Path	Incidence Angle (°)
1	2 April	stripmap	HH/VV	SSC	Right	Descending	39
2	24 April	stripmap	HH/VV	SSC	Right	Descending	39
3	5 May	stripmap	HH/VV	SSC	Right	Descending	39
4	18 June	stripmap	HH/VV	SSC	Right	Descending	39

Three eight-band multispectral Landsat 8 images from 13 April, 29 April, and 16 June 2016, with a resolution of 30 m were used to aid in visual comparison and validation of the TSX data (Figure 2). It is important to note the change in ice cover between the 13 April scene and the 29 April scenes. By the 16 June scene, the vegetation canopy is fully developed, shown in green. In the 29 April scene, cloud cover can be noticed, which is a clear limitation of optical imagery. In situ data of the region does not exist, which means that the classification results have to be validated based on the satellite image only. Hydrometric data for Lac Simon and Lac Schryer exist only until 2006, which is before the SAR scenes were acquired. This compromises the evaluation of the absolute performance of the classification methods, however, the relative comparison reveals performance differences that can be validated with existing knowledge of the land cover types and the satellite imagery in the area.

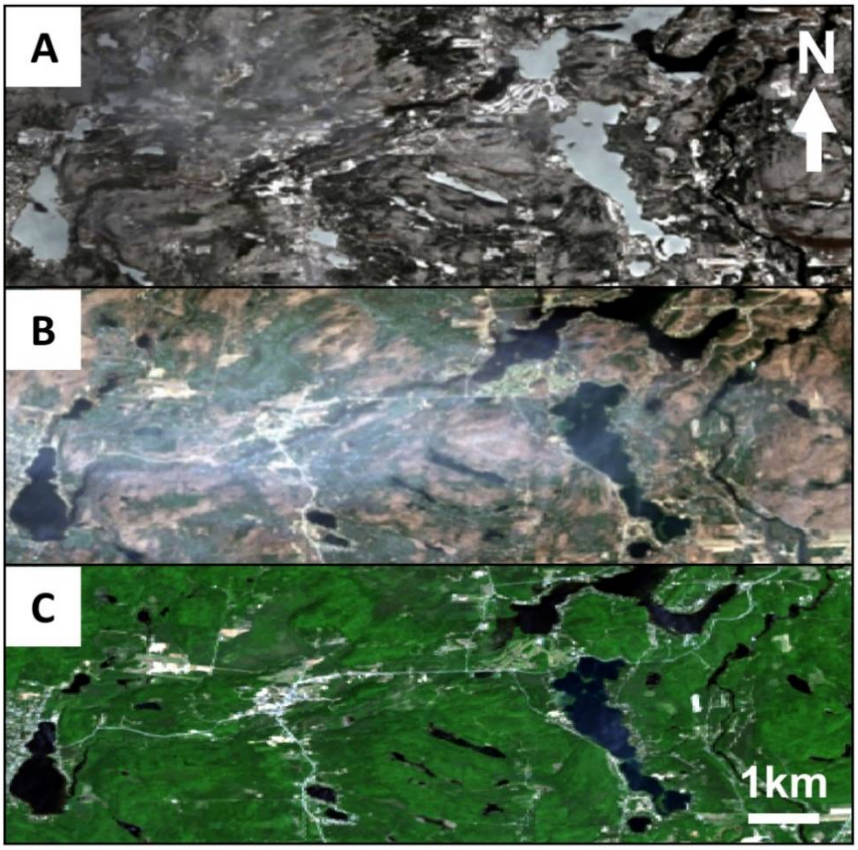

Figure 2. Time series of Landsat 8 true colour optical images (red-green-blue (RGB): 4-3-2) from the following scenes: (**A**) 13 April 2016; (**B**) 29 April 2016; and (**C**) 16 June 2016.

2.2. Classification Methods

Each TSX scene was processed using three different methods: grey-level thresholding applied to single-polarization data (HH), the Kennaugh Element Framework [27] applied to dual-polarization data (HH, VV), and H-Alpha-Dual-Polarization decomposition (HH, VV). The processing workflow for each method can be seen in Figure 3.

The HH band of the TSX data was used to simulate single-polarization data. HH polarization tends to be used over HV or VV, because the difference in backscatter response between land and water are greatest for HH polarization [4,17,28–31]. Grey-level thresholding was used to classify each SAR scene because it is a simple and effective way to map surface water [7,32]. Because the histogram of the intensity data is bimodal, a value in between the two modes can be chosen, in which everything below this threshold is classified as water and everything above is classified as non-water. In this study, the threshold value used was the minimum between the two modes. This method was applied to all

four TSX images, producing four models each with two classes (water and other). The processing work flow for this method is shown in Figure 3. The processing software used herein included SNAP, Matlab code developed in house, and the Kennaugh Element Framework by Schmitt et al. [27]. The Shuttle Radar Topography Mission (SRTM) finished Digital Elevation Model (DEM) was used for the terrain correction and standard speckle filters were applied.

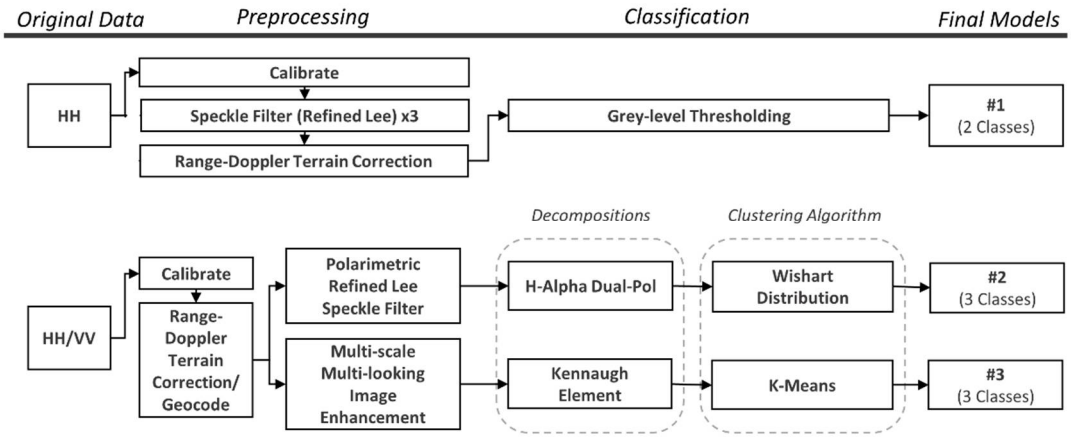

Figure 3. Processing workflow for single- and dual-polarization data to create three final models for each TerraSAR-X (TSX) scene.

Studies have shown successful results using dual-co-polarization HH/VV data for flooded vegetation mapping [18,20,33]. Several common decomposition types exist to break down the data into polarimetric parameters, but there are few that are adapted for dual-polarization data. In this study, two dual-polarization decompositions will be used to classify water and flooded vegetation. The first is the H-Alpha decomposition, which was developed in 2007 and modified for dual-polarization data [34]. The second method is the Kennaugh Element Framework developed by Schmitt et al. [27]. A few studies have researched the use of this technique for mapping wetlands and have proved it successful [18,26,27].

The H-Alpha decomposition for dual-polarization data uses an eigenvector analysis of the coherency matrix [T2], which separates the parameters into scattering processes (the eigenvectors) and their relative magnitudes (the eigenvalues) [34]. There are two parameters outputted from the H-Alpha decomposition, entropy (H) and alpha (α). Entropy is calculated from the eigenvalue information and represents the degree of randomness in the scattering. Alpha (α) is calculated from the eigenvectors and represents a rotation that can indicate the type of scattering mechanism [35]. Figure 4 shows the entropy and alpha parameters for the scene of 2 April 2016. Water is shown with orange colors in Figure 4A (entropy), while ice is shown in blue colors. The alpha parameter shows water along the river, but does not outline the ice-covered regions in the scene. In combination, entropy and alpha parameters are able to distinguish water- and ice-covered areas. The quad-polarization decomposition of H-Alpha has shown to work well in natural environments, because this method is an incoherent decomposition that can characterize distributed targets [1]. However, the modified dual-polarized H-Alpha decomposition is less well-studied. The unsupervised Wishart distribution clustering algorithm is applied to the H-Alpha decomposition, as the coherency matrix can be modelled by this algorithm. The Wishart distribution is robust and can be applied to any type of polarimetric SAR data, so it is often applied to the H-Alpha decompositions (dual or quad) [1]. Nine different classes were created using the Wishart classifier on the H-Alpha decomposition. These classes were visually inspected to determine which classes could be re-clustered to represent the desired three classes; (i) open water, (ii) flooded vegetation, and (iii) other. This processing method was applied to all four TSX images, producing four models each with three classes (Figure 3).

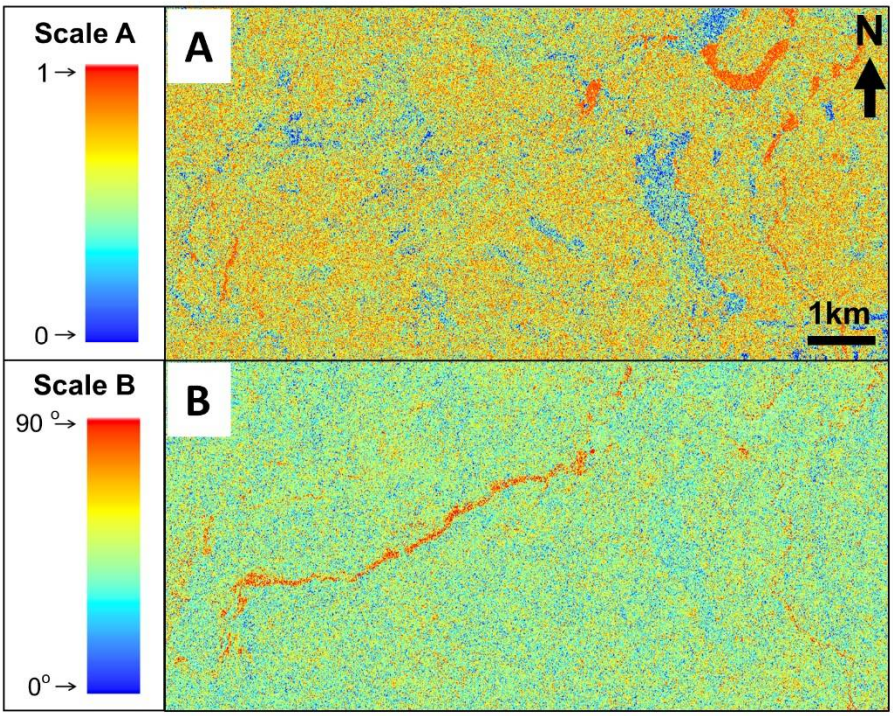

Figure 4. Images of parameters entropy (**A**) and alpha (**B**) for the TerraSAR-X scene from 2 April 2016.

The Kennaugh Element Framework developed by Schmitt et al. [27] linearly transforms the four-dimensional Stokes vector into a four-by-four scattering matrix, called the Kennaugh matrix [K]. Four normalized Kennaugh elements from this matrix K can be computed using dual-co-polarization data. In the case of HH/VV data, the elements are K_0, K_3, K_4, and K_7. K_0 represents the total intensity as a sum of HH and VV intensity; K_3 represents the difference between double-bounce and surface intensity; K_4 represents the difference between HH and VV intensity; and K_7 represents the phase shift between double-bounce and surface scattering mechanisms. These four elements have been shown to be very useful for identifying flooded vegetation. A study by Moser et al. [25] has demonstrated that open water has low values of K_0, because of the specular scattering nature of calm water causing a low backscatter signature. These areas generally form clusters that can be distinctly separated from the other classes. Flooded vegetation is characterized by high values of K_4, medium values of K_3 and lower values of K_0. Another study identified the significant difference between HH and VV intensity over flooded areas and inundated forests, emphasizing the importance of K_4 [36]. Using a pre-process Kennaugh chain, the Kennaugh elements were geocoded, calibrated, and enhanced using a multi-scale and multi-looking technique developed by Schmitt [37] (Figure 3). An example of the four Kennaugh elements produced for the 2 April 2016 scene can be seen in Figure 5. This scene was selected as it exhibits open water, ice cover, inundated vegetation, and other land cover. Open water is represented by the lowest values of K_0 (dark blue in Figure 5A) and medium values of K_3 (grey in Figure 5B). Flooded vegetation is represented by medium values of K_3 (grey and yellow in Figure 5B) and high values of K_4 (red and yellow in Figure 5C). Additionally, K_7 (Figure 5D), representing the phase shift between double-bounce and surface scattering, shows sensitivity to inundated vegetation, although not as strong as K_4, which was already found by Zalite et al. [36]. Ice cover is represented by low values of K_0 (light blue in Figure 5A) and low values of K_3 (dark blue in Figure 5B). These elements were processed using an unsupervised k-means classifier. The k-means clustering algorithm is one of the simplest forms of clustering techniques that aims at minimizing the Euclidean distance between points. The advantages of this technique are that it is fast and robust, and thus works well when applied to large, linear data sets, such as the Kennaugh elements. The k-means classifier produced 11 classes that

were then visualized and analyzed to determine which classes represented (i) open water, (ii) flooded vegetation, and (iii) other. This processing method was applied to all four TSX images, producing four models each with three classes.

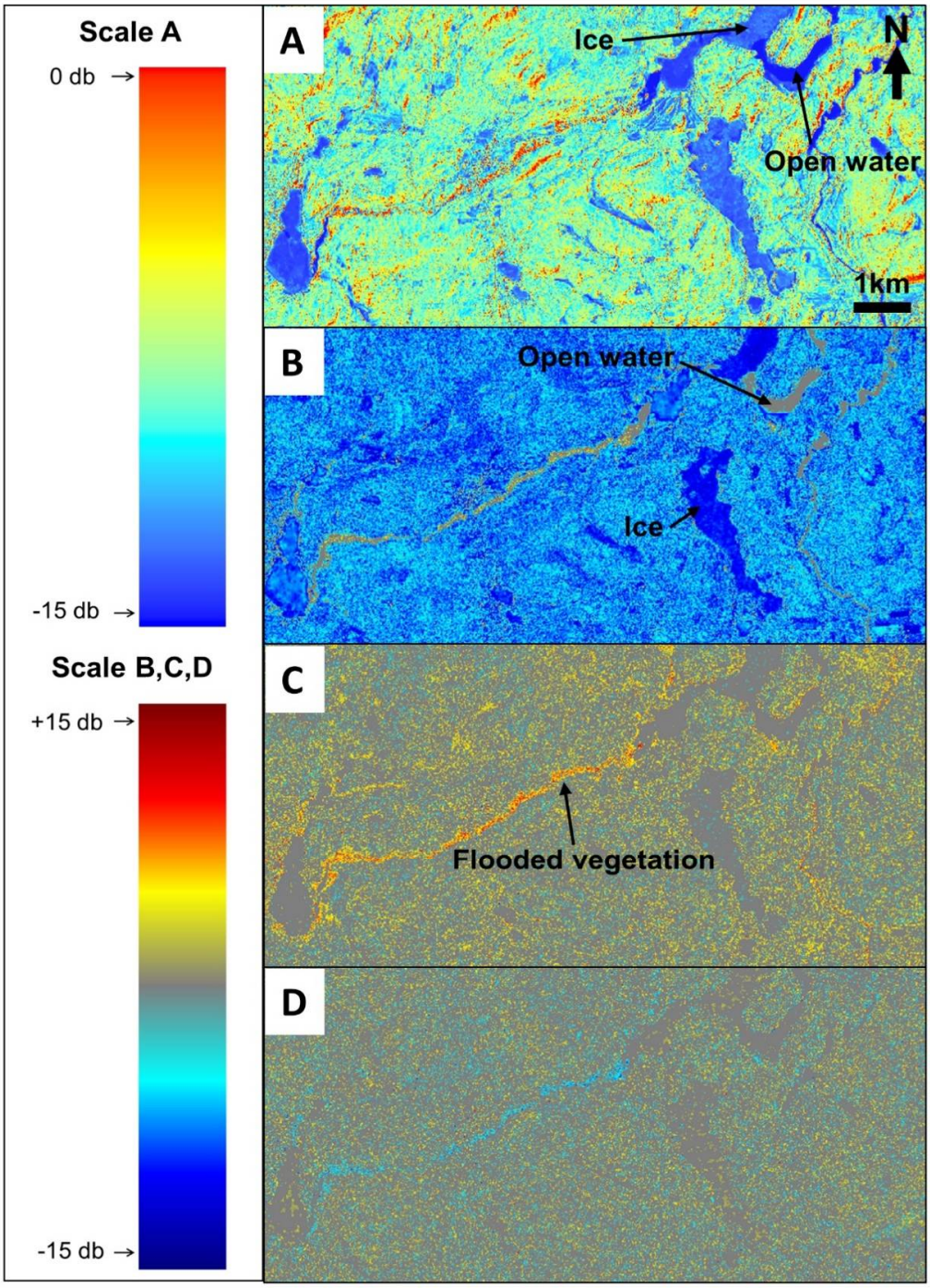

Figure 5. Four Kennaugh elements derived from the dual-pol TerraSAR-X image from 2 April 2016. (**A**) K_0—the total intensity sum of HH plus VV; (**B**) K_3—difference double-bounce minus surface scattering; (**C**) K_4—difference HH minus VV intensity; (**D**) K_7—phase shift between double-bounce and surface scattering mechanisms. Open water is represented by dark blue in (**A**) and grey in (**B**). Flooded vegetation is represented by grey and yellow in (**B**) and red and yellow in (**C**). Ice cover is represented by light blue in (**A**) and dark blue in (**B**). Inundated vegetation is shown in yellow/red in (**C**) and cyan in (**D**).

3. Results

3.1. Single Polarization Classification

The four water classification models created using grey-level thresholding can be seen in Figure 6. Areas of black represent water and grey areas represent non-water. Table 2 outlines the percentages of the two classes through time, as well as the threshold value used. Water classification changes from 8% to 10% throughout the four scenes, disagreeing with seasonal trends, which should show an increase in temperature causing a decrease in water. However, several other processes are occurring to account for this change. Ice can be seen in only the first scene (blue box in Figure 6A), as it is classified as both other and water, and decreases the amount of total water classified. The marsh land shown in the red box in Figure 6 is flooded in the first scene (A), but dried out by the last scene (D). This change agrees with seasonal change, despite the overall trend of water classification showing an increase. Counteracting this seasonal drying is an increase in overall misclassification in the first scene (A), as a result of ice and snow, and last scene (D), as a result of vegetation growth (shown in the yellow box in Figure 6). Although the single-polarization methodology was able to see seasonal changes in some wetlands, flooded vegetation was not classified, and misclassification errors occurred as a result of ice and tall vegetation causing an incorrect interpretation of the total surface water change in the area, a clear limitation of using single-polarization data only.

Table 2. Percentages of each class and threshold values used in each TerraSAR-X (TSX) scene using grey-level thresholding.

Date (2016)	Threshold Value (dB)	Water (%)	Other (%)
2 April	−17.38	8	92
24 April	−19.68	9	91
5 May	−18.56	10	90
18 June	−18.87	10	90

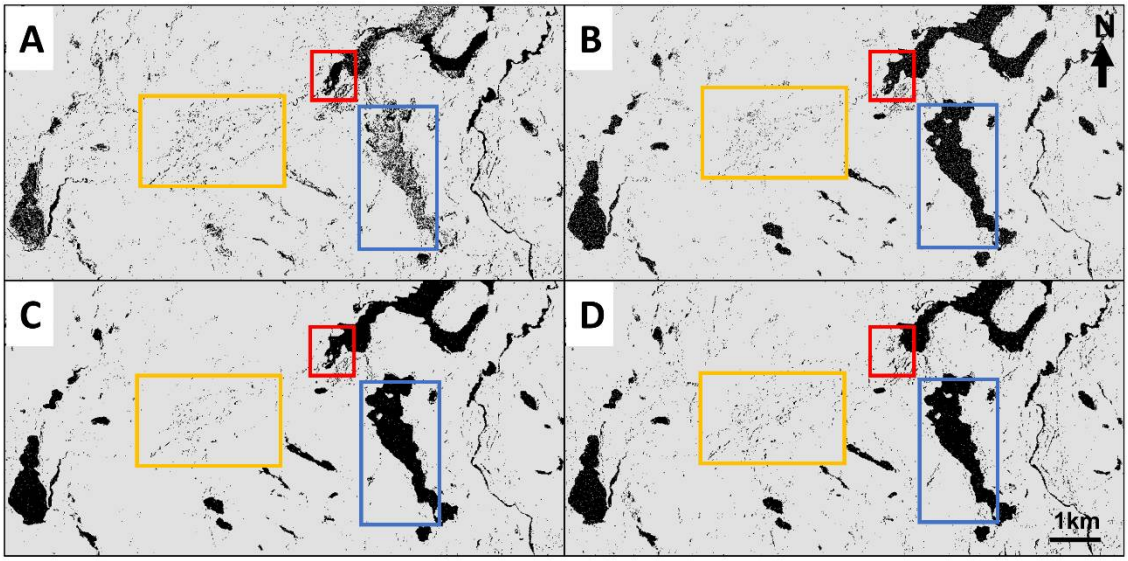

Figure 6. Grey-level thresholding classified models showing water (black) and other (grey) for (**A**) 2 April 2016; (**B**) 24 April 2016; (**C**) 5 May 2016; and (**D**) 18 June 2016. Coloured boxes indicate example areas of temporal change: blue—ice melting; red—marshland dries out; yellow—areas of misclassification due to ice (**A**) and vegetation (**C**).

3.2. Dual-Polarization Classification: H-Alpha–Wishart

The water classification models created using the unsupervised H-Alpha–Wishart classification can be seen in Figure 7, showing three classes: water (black), flooded vegetation (blue), and other (grey). Of the original nine classes, each model consistently identified Class 3 (blue) as flooded vegetation and Class 7 (black) as open water.

Table 3 display the results for each scene classified using the H-Alpha–Wishart method. The percent of water classified gradually decreases from the first scene until the last scene. This is expected as the seasonal changes from wet to dry occur during the study time period. However, some areas are misclassified as water, including a golf course located south of the Baie-de-l'Ours present in the optical imagery (blue box in Figure 7). Some fields identifiable in the optical imagery are classified as water as well (black areas in yellow box in Figure 7). The percent of flooded vegetation stays around approximately 5%, which is inconsistent with season trends. However, in the April scenes (A and B), there is flooded vegetation centered on the river, whereas this disappears in the later scenes (yellow box in Figure 7). The marsh area seen in the red box is shown to dry up in the final scene (D), which is consistent with the single-polarization SAR observations. Ice is not differentiable from open water in the first scene. The sum of water and flooded vegetation (total surface water) decreases and is consistent with the expected seasonal change. Some areas (yellow box in Figure 7) that are classified as water on 5 May (C) are classified as flooded vegetation on 18 June (D). This is an indication that vegetation changes may lead to a change in class, but not a change from water to non-water. Hence, the classification of total surface water seems more robust than the discrimination of open water and flooded vegetation. As the vegetation starts developing in May and is fully developed in June, the change in class could be a consequence of that. It is worth noting that snow fall occurred in the area throughout April, which may have led to snow and ice being misclassified as flooded vegetation in both April scenes. A rise in temperature by 15–20 degrees in early May may have melted the snow and ice, which became classified as water, considering that leafs have not developed yet. By June, vegetation has developed in and around water bodies, indicated by the increasing areas of classified flooded vegetation in the scene.

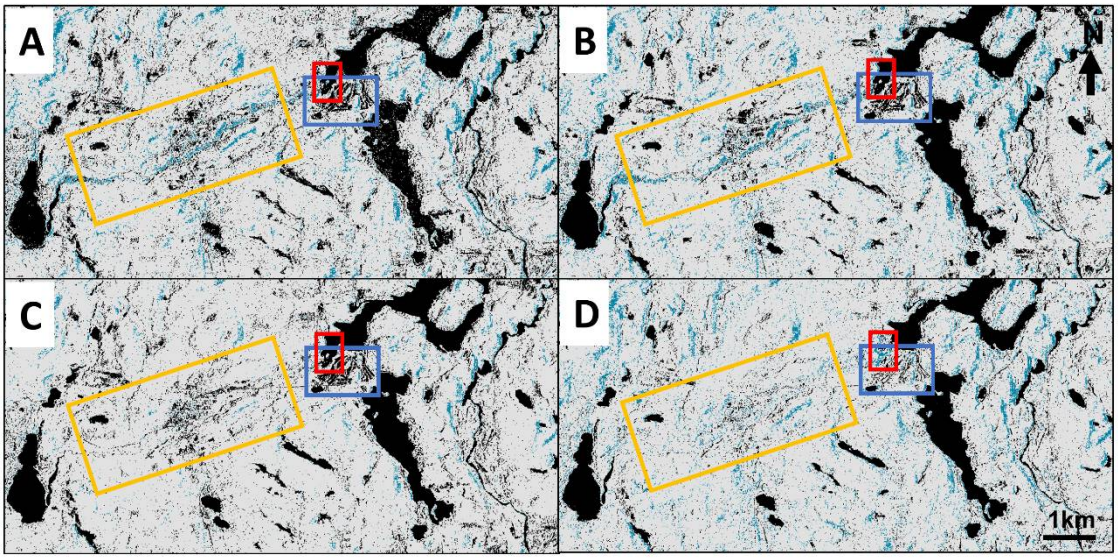

Figure 7. H-Alpha–Wishart classified models showing water (black), flooded vegetation (blue), and other (grey) for (**A**) 2 April 2016; (**B**) 24 April 2016; (**C**) 5 May 2016; and (**D**) 18 June 2016. Coloured boxes indicate example areas of change: blue—golf course misclassified as water; red—marshland dries out; yellow—flooded vegetation decreases, and misclassification of fields.

Table 3. Percentages of each class identified for each H-Alpha–Wishart model through time.

Date (2016)	Water (%)	Flooded Vegetation (%)	Other (%)
2 April	17	5	78
24 April	15	6	79
5 May	16	2	82
18 June	12	6	82

3.3. Dual-Polarization Classification: Kennaugh Element Framework

A time series of the four false colour composites of the processed Kennaugh elements, K_3-K_0-K_4, are shown in Figure 8. Colours are used to clearly differentiate the four classes. Bright pink represents open water; white/light pink colour represents flooded vegetation; green and blue represent the 'other' class, which includes forest, urban areas, agricultural land, or other classifications of land. The dark purple colour seen in the 2 April scene represents ice, which corresponds to the optical imagery.

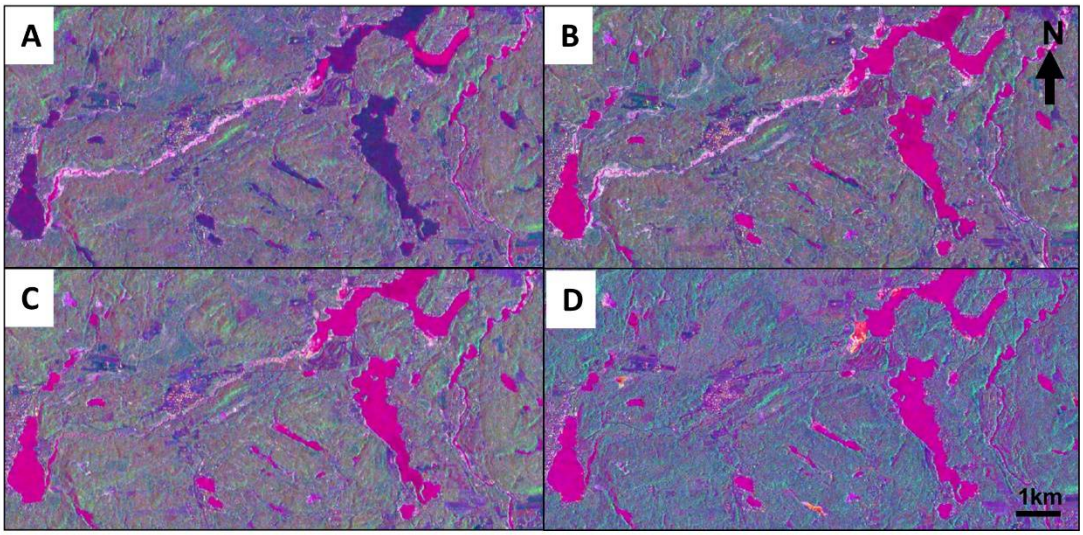

Figure 8. False colour composites of the processed Kennaugh elements, K_3-K_0-K_4, from (**A**) 2 April, (**B**) 24 April, (**C**) 5 May, and (**D**) 18 June 2016. Open water appears in pink, ice in dark purple, flooded vegetation in white/light pink, and 'other' in green and blue.

The Kennaugh element technique agrees with the optical imagery. The ice can be seen to disappear by the end of April and the water bodies are consistent. The Kennaugh elements were able to observe the flooded vegetation during melting, especially in the first two scenes, which the optical imagery was not able to identify. The Kennaugh elements were then classified using an unsupervised k-means classifier. This developed 11 classes for each scene. The average of each class of each Kennaugh element was analyzed and results are shown in Figure 9. It shows three plots, K_0 versus K_4, K_3 versus K_4, and K_0 versus K_3, for each of the four scenes. Using this technique, each point was assigned one class of three possible classes; open water, flooded vegetation, and other. It can be seen that the points assigned as water were consistently the lowest value of K_0. Flooded vegetation was consistently identified as the highest value in K_4. These findings are consistent with Moser et al. [25].

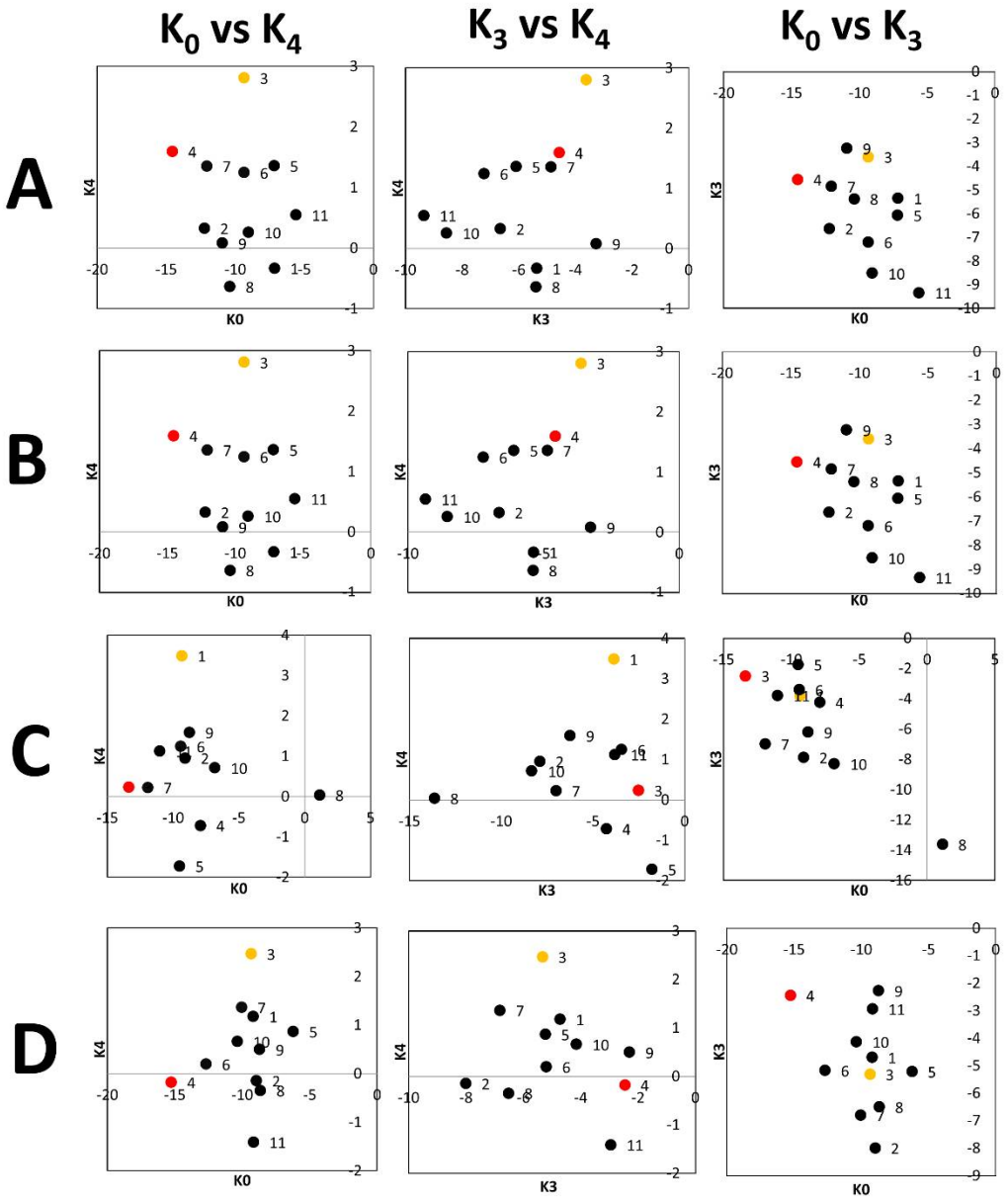

Figure 9. Graphs of the average of each class for the Kennaugh elements used to classify water (red), flooded vegetation (yellow), and other (black). (**A**) 2 April 2016; (**B**) 24 April 2016; (**C**) 5 May 2016; and (**D**) 18 June 2016.

The water classification models for each of the four scenes can be seen in Figure 10. Table 4 outlines the percentages of each class identified through time. The black areas represent open water and are shown to decrease from the first scene to the last scene from 16% to approximately 12%. However, in the first scene (green box in Figure 10A), the water is distributed and lakes are classified as both other and water, indicating the presence of ice. The flooded vegetation (blue) decreases from 13% to 5% with time. This corresponds with the seasonal melt that would occur in the first two scenes in early spring, and the seasonal drying that could occur during late spring and early summer of the last two scenes. Similar to H-Alpha–Wishart, misclassification of flooded vegetation can be seen distributed throughout the scene. However, the flooding around the river is evident in the first two scenes and not the last two (yellow box in Figure 10). A golf course south of Baie-de-l'Ours is misclassified as water (see Figure 1B), which is not seen in the optical imagery (blue box in Figure 10). Finally, the marsh area seen in the red box shows a drying out in the last scene similar to the other two classification methodologies.

Table 4. Percentages of each class identified for each Kennaugh Element model through time.

Date (2016)	Water (%)	Flooded Vegetation (%)	Other (%)
2 April	16	13	72
24 April	12	13	75
5 May	13	5	82
18 June	12	5	83

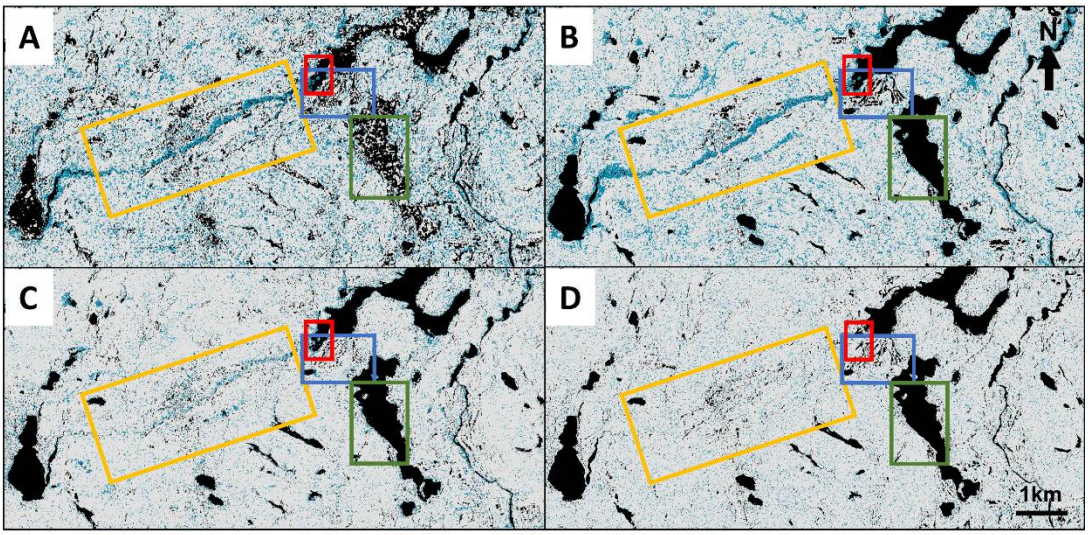

Figure 10. Kennaugh Element models classified showing water (black), flooded vegetation (blue), and other (grey) for (**A**) 2 April 2016; (**B**) 24 April 2016; (**C**) 5 May 2016; and (**D**) 18 June 2016. Coloured boxes indicate example areas of change: blue—golf course misclassified as water; red—marshland dries with time; yellow—flooded vegetation decrease, and misclassification of field areas; green—ice melting.

Differential Kennaugh elements [26] use the differences between the Kennaugh elements of two scenes to understand how the landscape has changed with time. This technique was applied to the first (2 April) and last (18 June) scene and can be seen in Figure 11. Each colour represents a type of change. Green represents the change from ice to open water, which is mainly reflected as a change in K_0 showing a decrease in total intensity. Dark red represents the change from flooded vegetation to land and accounts for a decrease in the difference between double-bounce and surface scattering or K_3. Yellow represents the change from open water to flooded vegetation, which is shown as an increase in K_3. This technique proves extremely useful, especially when comparing open water and flooded vegetation, because a clear distinction can be seen. The ability to identify the change from ice cover to open water is also important as it can indicate when the first seasonal melt and flooding occurs.

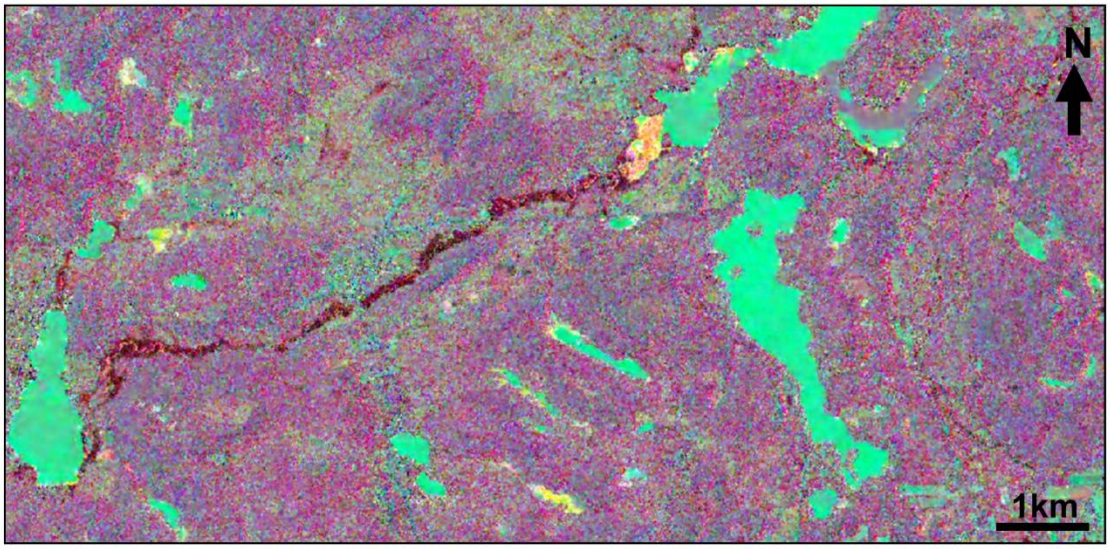

Figure 11. False colour composite of the differential Kennaugh elements, K_0-K_3-K_4, differenced between the 18 June 2016 scene and the 2 April 2016 scene. Red represents the change from flooded vegetation to land. Green represents the change from ice to open water. Yellow represents the change from open water to marshland.

4. Discussion

A comparison of the three methods, k-means performed on the Kennaugh elements, unsupervised H-Alpha–Wishart classification, and grey-level thresholding, can be seen in Figure 12. All methods were able to classify open water, however, the dual-polarization methods consistently classified more water than the grey-level thresholding technique. This was unexpected as the single-polarization data often have errors of commission from shadow zones classified as water. However, more misclassification occurred in the dual-polarization methods, including classifying fields and a golf course as water. Both of the dual-polarization methods show the correct decreasing trend of water over the study period from April to June 2016 that one would expect to see, including seasonal melting. The results from thresholding disagree with this and show a slight increase over time from 8% to 10%. No classification method was able to classify ice in a single class in the 2 April scene, however, grey-level thresholding and the Kennaugh Element k-means classifier were able to classify some portion of the ice covered lakes as other. Both dual-polarization methods were able to identify flooded vegetation. However, the Kennaugh elements classifier sees a decrease in flooded vegetation with time, which agrees better with seasonal trends. Both methods were able to classify the river flooding in the April scenes and no flooding occurring in the later scenes. The single-polarization method was unable to classify flooded vegetation, and instead classified it as other or non-water. The findings presented here are in line with the results of Mleczko and Mroz [38], who compared Sentinel-1 and Tandem-X multi-polarization data and concluded that dual polarization of TanDEM-X achieves the best results, while full polarization shows only marginally better performance for wetlands and flooded vegetation. Hence, full polarimetric acquisitions may not be efficient or needed for wetland mapping. Alternative classification procedures, such as Shannon Entropy [23] and interferometric coherence, have not shown to yield better results, unless full polarimetric coherence is used for simultaneous image acquisition by TerraSAR-X and Tandem-X [38]. Other studies using dual-polarimetric TerraSAR-X acquisitions and a variety of polarimetric indices demonstrate the strong dependence of the indices on vegetation conditions [39]. The performance of polarimetric indices thus depends on seasonal conditions, which mandates a classification technique such as differential Kennaugh elements, which is able to determine the change between different land cover classes throughout the available acquisition time period. An additional valuable parameter for

water classification would be water levels, which have successfully been determined from wetland in SAR [40]. Multi-frequency acquisitions from different satellites, in combination with Kennaugh element decomposition, has also shown great potential for discriminating different vegetation types (e.g., [41]).

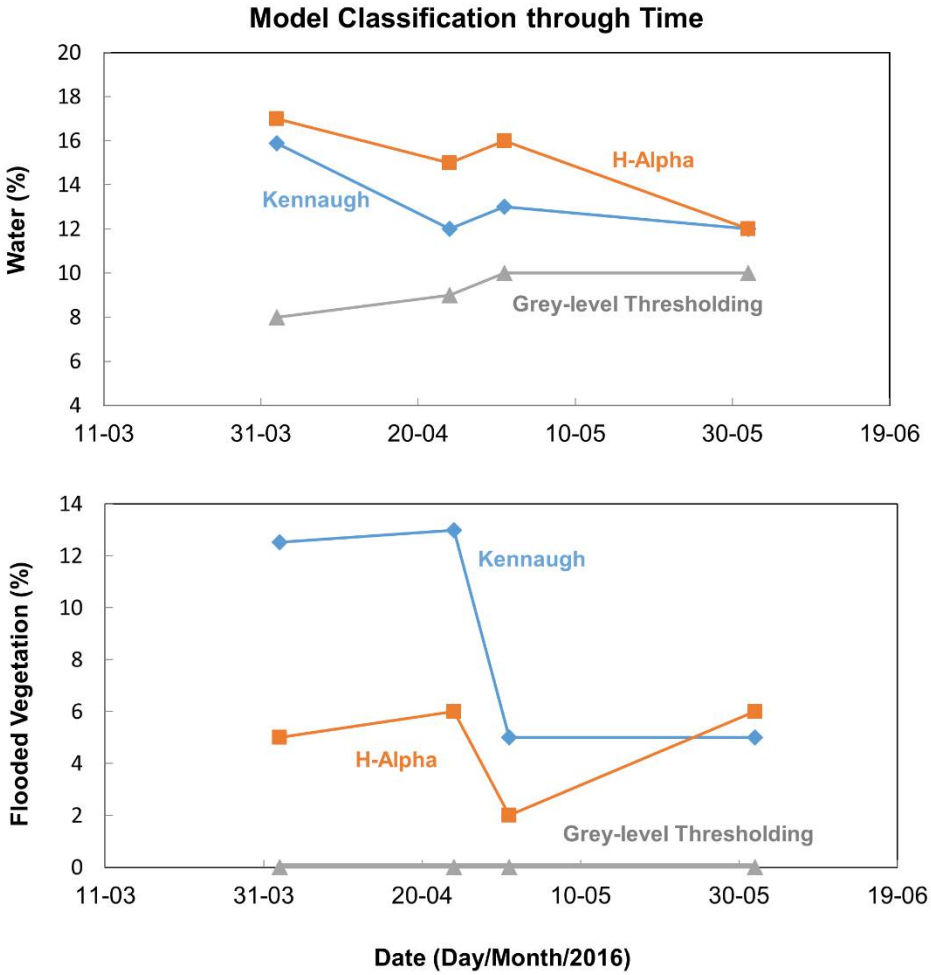

Figure 12. Graphs showing percent of water and percent of flooded vegetation classified through time for each of the classification methods. Lines: Blue diamond—unsupervised k-means classification on Kennaugh Elements, orange square—H-Alpha–Wishart unsupervised classification, and grey triangle—grey-level thresholding.

5. Conclusions

In this study, three different SAR classification methods were used to identify areas of water, ice, and flooded vegetation in four TSX scenes over a principally natural landscape. A river, which is seasonally flooded in the centre of the study area, serves as a test-bed for these methodologies. Single-polarization grey-level thresholding is an established technique for surface water monitoring and has the capability to classify areas of water and non-water. Using the techniques of H-Alpha–Wishart and the Kennaugh Element Framework applied to dual polarization data, the ability to analyze scattering mechanisms and classify water and flooded vegetation was tested and compared with the single-polarization method.

The H-Alpha–Wishart unsupervised classification for dual-polarization data was able to classify areas of open water and flooded vegetation. Flooded vegetation was classified surrounding the river in the first two scenes acquired in April, and not in the last two scenes acquired in May and

June. This corresponds with optical imagery of the same time period. This classifier was not able to distinguish areas of ice in the first scene, and misclassified them as open water.

The Kennaugh Element Framework was able to classify areas of open water, flooded vegetation, and ice. K_4 was used to distinguish areas of flooded vegetation and K_0 was used to identify areas of open water. Similar conclusions were found by Moser et al. [25]. The differential Kennaugh analysis on all four elements, looking at the difference from the first scene to the last scene, was able to indicate where changes occurred, as well as what changes occurred. The change between ice and open water, open water and marshland, and flooded vegetation and land were clearly identified using this method. Applying the k-means classifier allowed for the classification of open water and flooded vegetation which agreed with seasonality, but the areas of ice cover are less well-defined.

Finally, the single-polarization grey-level thresholding method proved to identify open water well. Part of the lakes were classified as other in the first scene, which indicates the potential to classify ice (or rather not misclassify water). However, the total surface water in each scene shows little change and no seasonal variation compared to the result of the Kennaugh Element Framework, which shows a decrease in flooded vegetation from 12% to 5%, indicating a seasonal change from flooding to drying. These conclusions could not have been drawn from the single-polarization data and, therefore, a clear advantage to dual-polarization data is the ability to show seasonal fluctuations. In addition, dual-polarization is able to distinguish open water and flooded vegetation.

The findings of this study confirm the expected advantages of dual-polarization observations, however, single-polarization observations are still useful in classifying water, albeit not sufficiently for identifying seasonal changes in vegetated areas. The applicability of single-polarization SAR for landscape dynamics is thus limited. Considering potential applications in earth system monitoring and process understanding, where not only the land cover type, but also the spatio-temporal transition from one type to another is highly relevant, the use of dual-polarization (or multi-polarization for specific land cover types) SAR data is a necessity.

Author Contributions: The research conducted and described in this manuscript was performed by all co-authors. Specifically, the following contributions were made: "Conceptualization, K.I., A.B., A.R.; Methodology, K.I., B.W., A.R.; Validation, K.I., A.R.; Resources, G.F., A.B., A.R.; Writing—Original Draft Preparation, K.I., G.F.; Writing—Review & Editing, K.I., G.F., A.B., A.R., B.W.; Visualization, K.I., A.B.; Supervision, G.F., A.B., A.R."

Funding: The German Space Agency (DLR) is acknowledged for providing TerraSAR-X data. NSERC is acknowledged for partially funding this research.

Conflicts of Interest: The authors declare no conflict of interest.

References

1. Lee, J.-S.; Pottier, E. *Polarimetric Radar Imaging: From Basics to Applications*; CRC Press: Boca Raton, FL, USA, 2009; 422p. [CrossRef]
2. Lee, J.-S.; Grunes, M.R.; Pottier, E. Quantitative Comparison of Classification Capability: Fully Polarimetric versus Dual and Single-Polarization SAR. *IEEE Trans. Geosci. Remote Sens.* **2001**, *39*, 2343–2351. [CrossRef]
3. Brisco, B.; Touzi, R.; van der Sanden, J.J.; Charbonneau, F.; Pultz, T.J.; D'Iorio, M. Water Resource Applications with RADARSAT-2—A Preview. *Int. J. Digit. Earth* **2008**, *1*, 130–147. [CrossRef]
4. White, L.; Brisco, B.; Dabboor, M.; Schmitt, A.; Pratt, A. A Collection of SAR Methodologies for Monitoring Wetlands. *Remote Sens.* **2015**, *7*, 7615–7645. [CrossRef]
5. Kuenzer, C.; Guo, H.; Huth, J.; Leinenkugel, P.; Li, X.; Dech, S. Flood Mapping and Flood Dynamics of the Mekong Delta: ENVISAT-ASAR-WSM Based Time Series Analyses. *Remote Sens.* **2013**, *5*, 687–715. [CrossRef]
6. Schlaffer, S.; Matgen, P.; Hollaus, M.; Wagner, W. Flood Detection from Multi-Temporal SAR Data Using Harmonic Analysis and Change Detection. *Int. J. Appl. Earth Obs. Geoinf.* **2015**, *38*, 15–24. [CrossRef]
7. White, L.; Brisco, B.; Pregitzer, M.; Tedford, B.; Boychuk, L. RADARSAT-2 Beam Mode Selection for Surface Water and Flooded Vegetation Mapping. *Can. J. Remote Sens.* **2014**, *40*, 135–151. [CrossRef]
8. Martinis, S.; Kersten, J.; Twele, A. A Fully Automated TerraSAR-X Based Flood Service. *ISPRS J. Photogramm. Remote Sens.* **2015**, *104*, 203–212. [CrossRef]

9. Mason, D.C.; Speck, R.; Devereux, B.; Schumann, G.; Neal, J.C.; Bates, P.D. Flood Detection in Urban Areas Using TerraSAR-X. *IEEE Trans. Geosci. Remote Sens.* **2010**, *48*, 882–894. [CrossRef]
10. Matgen, P.; Schumann, G.; Henry, J.B.; Hoffmann, L.; Pfister, L. Integration of SAR-Derived River Inundation Areas, High-Precision Topographic Data and a River Flow Model toward near Real-Time Flood Management. *Int. J. Appl. Earth Obs. Geoinf.* **2007**, *9*, 247–263. [CrossRef]
11. Liu, H.; Jezek, K.C. Automated Extraction of Coastline from Satellite Imagery by Integrating Canny Edge Detection and Locally Adaptive Thresholding Methods. *Int. J. Remote Sens.* **2004**, *25*, 937–958. [CrossRef]
12. Imhoff, M.L.; Vermillion, L.; Story, M.H.; Choudhury, A.M.; Gafoor, A.; Polcyn, F. Monsoon Flood Boundary Delineation and Damage Assessment Using Space Borne Imaging Radar and Landsat Data. *Photogramm. Eng. Remote Sens.* **1987**, *53*, 405–413.
13. Mason, D.C.; Horritt, M.S.; Dall'Amico, J.T.; Scott, T.R.; Bates, P.D. Improving River Flood Extent Delineation from Synthetic Aperture Radar Using Airborne Laser Altimetry. *IEEE Trans. Geosci. Remote Sens.* **2007**, *45*, 3932–3943. [CrossRef]
14. Martinis, S.; Twele, A.; Voigt, S. Towards Operational near Real-Time Flood Detection Using a Split-Based Automatic Thresholding Procedure on High Resolution TerraSAR-X Data. *Nat. Hazards Earth Syst. Sci.* **2009**, *9*, 303–314. [CrossRef]
15. Giustarini, L.; Chini, M.; Hostache, R.; Pappenberger, F.; Matgen, P. Flood Hazard Mapping Combining Hydrodynamic Modeling and Multi Annual Remote Sensing Data. *Remote Sens.* **2015**, *7*, 14200–14226. [CrossRef]
16. Irwin, K.; Beaulne, D.; Braun, A.; Fotopoulos, G. Fusion of SAR, Optical Imagery and Airborne LiDAR for Surface Water Detection. *Remote Sens.* **2017**, *9*, 890. [CrossRef]
17. Gstaiger, V.; Huth, J.; Gebhardt, S.; Wehrmann, T.; Kuenzer, C. Multi-Sensoral and Automated Derivation of Inundated Areas Using TerraSAR-X and ENVISAT ASAR Data. *Int. J. Remote Sens.* **2012**, *33*, 7291–7304. [CrossRef]
18. Schmitt, A.; Brisco, B. Wetland Monitoring Using the Curvelet-Based Change Detection Method on Polarimetric SAR Imagery. *Water* **2013**, *5*, 1036–1051. [CrossRef]
19. Mermoz, S.; Allain-Bailhache, S.; Bernier, M.; Pottier, E.; Van Der Sanden, J.J.; Chokmani, K. Retrieval of River Ice Thickness from C-Band PolSAR Data. *IEEE Trans. Geosci. Remote Sens.* **2014**, *52*, 3052–3062. [CrossRef]
20. Brisco, B.; Schmitt, A.; Murnaghan, K.; Kaya, S.; Roth, A. SAR Polarimetric Change Detection for Flooded Vegetation. *Int. J. Digit. Earth* **2011**, *6*, 103–114. [CrossRef]
21. Gallant, A.L.; Kaya, S.G.; White, L.; Brisco, B.; Roth, M.F.; Sadinski, W.; Rover, J. Detecting Emergence, Growth, and Senescence of Wetland Vegetation with Polarimetric Synthetic Aperture Radar (SAR) Data. *Water* **2014**, *6*, 694–722. [CrossRef]
22. Hong, S.; Jang, H.; Kim, N.; Sohn, H.G. Water Area Extraction Using RADARSAT SAR Imagery Combined with Landsat Imagery and Terrain Information. *Sensors* **2015**, *15*, 6652–6667. [CrossRef] [PubMed]
23. Betbeder, J.; Rapinel, S.; Corgne, S.; Pottier, E.; Hubert-Moy, L. TerraSAR-X Dual-Pol Time-Series for Mapping of Wetland Vegetation. *ISPRS J. Photogramm. Remote Sens.* **2015**, *107*, 90–98. [CrossRef]
24. Dabboor, M.; White, L.; Brisco, B.; Charbonneau, F. Change Detection with Compact Polarimetric SAR for Monitoring Wetlands. *Can. J. Remote Sens.* **2015**, *41*, 408–417. [CrossRef]
25. Moser, L.; Schmitt, A.; Wendleder, A.; Roth, A. Monitoring of the Lac Bam Wetland Extent Using Dual-Polarized X-Band SAR Data. *Remote Sens.* **2016**, *8*, 302. [CrossRef]
26. Schmitt, A.; Leichtle, T.; Huber, M.; Roth, A. On the Use of Dual-Co-Polarized TerraSAR-X Data for Wetland Monitoring. *Int. Arch. Photogramm. Remote Sens. Spat. Inf. Sci. ISPRS Arch.* **2012**, *39*, 341–344. [CrossRef]
27. Schmitt, A.; Wendleder, A.; Hinz, S. The Kennaugh Element Framework for Multi-Scale, Multi-Polarized, Multi-Temporal and Multi-Frequency SAR Image Preparation. *ISPRS J. Photogramm. Remote Sens.* **2015**, *102*, 122–139. [CrossRef]
28. Hess, L.L.; Melack, J.M.; Filoso, S.; Wang, Y. Delineation of Inundated Area and Vegetation along the Amazon Floodplain with the SIR-C Synthetic Aperture Radar. *IEEE Trans. Geosci. Remote Sens.* **1995**, *33*, 896–904. [CrossRef]
29. Bourgeau-Chavez, L.L.; Kasischke, E.S.; Brunzell, S.M.; Mudd, J.P.; Smith, K.B.; Frick, L. Analysis of Space-Borne SAR Data for Wetland Mapping in Virginia Riparian Ecosystems. *Int. J. Remote Sens.* **2001**, *22*, 3665–3687. [CrossRef]

30. Townsend, P. A Synthetic Aperture Radar–based Model to Assess Historical Changes in Lowland Floodplain Hydroperiod. *Water Resour. Res.* **2002**, *38*. [CrossRef]
31. Manjusree, P.; Kumar, L.P.; Bhatt, C.M.; Rao, G.S.; Bhanumurthy, V. Optimization of Threshold Ranges for Rapid Flood Inundation Mapping by Evaluating Backscatter Profiles of High Incidence Angle SAR Images. *Int. J. Disaster Risk Sci.* **2012**, *3*, 113–122. [CrossRef]
32. Brisco, B.; Short, N.; Van Der Sanden, J.; Landry, R.; Raymond, D. A Semi-Automated Tool for Surface Water Mapping with RADARSAT-1. *Can. J. Remote Sens.* **2009**, *35*, 336–344. [CrossRef]
33. Kasischke, E.S.; Melack, J.M.; Dobson, M.C. The Use of Imaging Radars for Ecological Applications—A Review. *Remote Sens. Environ.* **1997**, *59*, 141–156. [CrossRef]
34. Cloude, S.R. The Dual Polarisation Entropy/Alpha Decomposition. In Proceedings of the 3rd International Workshop on Science and Applications of SAR Polarimetry and Polarimetric Interferometry, Frascati, Italy, 22–26 January 2007; pp. 1–6.
35. Cloude, S.R.; Pottier, E. A Review of Target Decomposition Theorems in Radar Polarimetry. *IEEE Trans. Geosci. Remote Sens.* **1996**, *34*, 498–518. [CrossRef]
36. Zalite, K.; Voormansik, K.; Olesk, A.; Noorma, M.; Reinart, A. Effects of Inundated Vegetation on X-Band HH-VV Backscatter and Phase Difference. *IEEE J. Sel. Top. Appl. Earth Obs. Remote Sens.* **2014**, *7*, 1402–1406. [CrossRef]
37. Schmitt, A. Multiscale and Multidirectional Multilooking for SAR Image Enhancement. *IEEE Trans. Geosci. Remote Sens.* **2016**, *54*, 5117–5134. [CrossRef]
38. Mleczko, M.; Mróz, M. Wetland Mapping Using SAR Data from the Sentinel-1A and TanDEM-X Missions: A Comparative Study in the Biebrza Floodplain (Poland). *Remote Sens.* **2018**, *10*, 78. [CrossRef]
39. Heine, I.; Jagdhuber, T.; Itzerott, S. Classification and Monitoring of Reed Belts Using Dual-Polarimetric TerraSAR-X Time Series. *Remote Sens.* **2016**, *8*, 552. [CrossRef]
40. Wdowinski, S.; Hong, S.H. Wetland InSAR: A review of the technique and applications. In *Remote Sensing of Wetlands Applications and Advances*; Tiner, R.W., Lang, M.W., Klemas, V.V., Eds.; CRC Press: Boca Raton, FL, USA, 2015; pp. 137–154. [CrossRef]
41. Ullmann, T.; Banks, S.N.; Schmitt, A.; Jagdhuber, T. Scattering characteristics of X-, C- and L-band PolSAR data examined for the tundra environment of the Tuktoyaktuk Peninsula, Canada. *Appl. Sci.* **2017**, *7*, 595. [CrossRef]